RSC Advances

This article can be cited before page numbers have been issued, to do this please use: Z. Ren, F. Zhang, L. Yue, X. Li, Y. Tao, G. Zhang, K. Wu, C. Wang and B. Li, *RSC Adv.*, 2015, DOI: 10.1039/C5RA05926G.

View Article Online
DOI: 10.1039/C5RA05926G

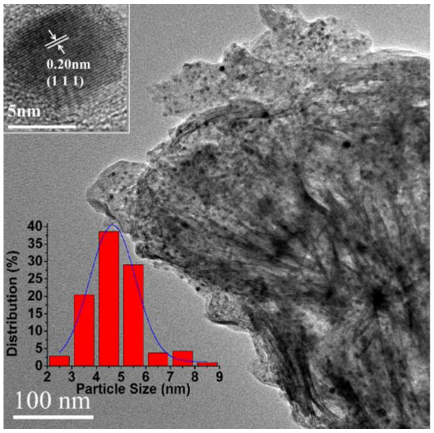

A series of highly dispersed nickel nanoparticles (with a uniform size about 4.7 nm) between the lamellae of silica pillared clay has been synthesized with a facile process. The nickel catalysts exhibit high catalytic performance on the hydrodechlorination of chlorobenzene, about 97.8% at 6% Ni-content, and better reusability.

View Article Online
DOI: 10.1039/C5RA05926G

Journal Name RSCPublishing

ARTICLE

Cite this: DOI: 10.1039/x0xx00000x

Received 00th January 2012,
Accepted 00th January 2012

DOI: 10.1039/x0xx00000x

www.rsc.org/

Nickel nanoparticles highly dispersed in the silica pillared clay as an efficient catalyst for chlorobenzene dechlorination

Zhiming Ren,[1] Fei Zhang,[3] Liwen Yue,[*2] Xuan Li,[4] Yu Tao,[4] Ge Zhang,[4] Kai Wu,[5] Cong Wang,[6] Baoshan Li[*1]

A series of highly dispersed nickel nanoparticles supported by silica pillared clay (SPC) have been synthesized with a facile process. The synthesized samples were characterized by XRD, HRTEM, SEM, IPC-ES, FTIR, N_2 adsorption–desorption isotherm and XPS techniques. The results suggest that the materials possess highly ordered mesoporous structure and the highly dispersed nickel nanoparticles with a uniform size about 4.7 nm are in an ordered configuration in the silica pillared clay's pores. Moreover, the nickel catalysts exhibit high catalytic performance on the hydrodechlorination of chlorobenzene, about 97.8% at 6 *wt.*% Ni-content, and better reusability.

1. Introduction

Metal nanoparticles, such as Ni, Pd, Pt, Au, and Rh, have received increasing attention due to their fascinating physical and chemical characteristics[1-6]. Compared with the conventional materials, nanoparticles exhibit smaller size, higher surface area and better activity etc[7,8]. Nickel nanoparticles, as a kind of metal nanoparticle, in recent years, have attracted more and more interesting, due to diverse promising applications in the fields of chemical catalysis for hydrogenation of nitrobenzene and nitrophenol, oxygen reduction, oxidation of olefins and hydrodechlorination of chlorobenzene[9].

Although, Ni nanoparticles have so many strong points, they have the same weak points as nanoparticles, such as the aggregation[10-11]. Therefore, many methods have been taken forward to protect the Ni nanoparticles from aggregation, keeping them in high activity, such as impregnating the Ni metal precursors into the zeolite[12], coating with SiO_2 around the Ni nanoparticles[13] , modified with polymers[14-19] and loading Ni nanoparticles on the surface of some metal oxides[20,21]. But the application of these methods in catalysts industry is very limited, because the preparation processes are complicated, expensive, and the size of the Ni-nanoparticles are hard to be controlled in a low level under those processes.

On the other hand, montmorillonite (MMT), as a kind of clay, is widely distributed in the entire world. It is cheap and easy to get. MMT possess layered structure, large surface area and high cation exchange capacity (CEC)[22,23]. Therefore, MMT is always used as the raw material for some valuable production, like organic clays[24], pillared clays[25,26], clay nanocrystalline composites, and clay-polymer composites[27]. It is worth to talk about the pillared clays. The pillared clays always arise from the combination of clays with metal and metal oxide materials, with micropores less than 2nm[28], which limited the application of the pillared clays very much. However, in the past several years, Mao [29-34] and his workers have developed the synthesis method of silica pillared clay (SPC). The synthesized SPC materials exhibit ordered mesoporous structure and large surface areas, even more than $1000m^2/g$. Moreover, the pore size of SPC is controllable by using different molecular length of surfactants. Furthermore, the synthesized condition is easy for industry. The application of pillared clays is then expanded to more different fields. If the Ni nanoparticles can be intercalated into the SPC, they would be much more stable, because the resultant composite structure can stabilize Ni nanoparticles and protect them from agglomeration, consequently, the catalytic efficiency of Ni nanoparticles can be elaborated. The weak points of Ni nanoparticles can be overcome. And the synthesized material will be cheap and easy to be industrialized.

In this research, we induced the Ni nanoparticles into the interlaminar of SPC by a two steps method and produce a kind of metal nano-material with the Ni nanoparticles highly dispersed in the mesoporous. The cost of the sample is cheap and the process of synthesis is easy to control, even if under the industry condition. In the first step, we synthesized the Ni^{II}-SPC, in which the nickel atoms were doped into the framework of SPC uniformly[32,35]. In the second step, the nickel atoms were reduced from the Ni^{II}-SPC precursor in hydrogen flow at a moderate temperature without destroying the structure of SPC. Finally, the Ni atoms are anchored to the framework of SPC, which ensures the nanoparticles be stable in the framework of SPC, preventing them from agglomeration. The catalytic performance of the result samples were examined by the reaction of HDC of CB. The significance of the work is that Ni nanoparticles can be highly dispersed in the structure of SPC with an ordered distribution and the result materials possess the advantages of SPC and Ni nanoparticles for catalysis, simultaneously.

2. Experimental Section

2.1 Materials

The natural montmorillonite clay (MMT) with a cation exchange capacity (CEC) of 91 meq/100 g was obtained from

View Article Online
DOI: 10.1039/C5RA05926G

Inner Mongolia and was used without any further purification or cationic-exchange process. Tetraethoxysilane (TEOS, A.R.) was purchased from West Long Chemical Co, Ltd., Guangdong, China. Dehydrated alcohol (A.R.), ammonia solution (25%) and was purchased from Beijing Chemical Plant, Beijing, China. Cetyltrimethylammonium bromide (CTAB, A.R.) and Nickel nitrate ($Ni(NO_3)_2 \cdot 6H_2O$, AR) were purchased from Beijing Yili Fine Chemical Product Limited Company, China.

2.2 Synthesis of Ni^{II}-SPC

0.5g of MMT was first dispersed in 20 mL de-ionized water, to which a certain amount of $Ni(NO_3)_2 \cdot 6H_2O$ was added and stirred for 30 min. At the same time, 0.5g of CTAB was dissolved in 2ml ethanol and 20ml de-ionized water, to which 3.7ml tetraethoxysilane (TEOS) was added and ultrasonic for 0.5 h to get emulsion. The emulsion was dropped into the clay dispersion slowly and stirred vigorously for 1.5h. Then deceleration stirred for 4.5h. Subsequently, 2ml of ammonia solution (25%) was added to it and continue stirring for 2h. The product was recovered by filtration and washed three times with de-ionized water. Finally the product was dried overnight at 105 °C. The samples were named Ni^{II}-SPC-6, Ni^{II}-SPC-3 and Ni^{II}-SPC-2, according to the amount of nickel added in this process were 6%, 3% and 2%, respectively.

2.3 Synthesis of Ni^0 -SPC

The synthesis of Ni^0-SPC by reduction of the Ni^{II}-SPC precursor was carried out as follow. Ni^{II}-SPC was put into a quartz tube and then heated in hydrogen flow from room temperature to 650 ^oC at a heating rate of 5 ^oC/min and kept 650 ^oC for 1 h. Then, it was cooled naturally in hydrogen flow to the room temperature. The resulting sample was designated as Ni^0-SPC.

2.4 Synthesis of SPC

The synthesis process of SPC was similar to that of Ni^{II}-SPC, and the only difference being that the $Ni(NO_3)_2 \cdot 6H_2O$ was not added to the MMT solution. After the product was dried overnight, the organic part was entirely removed from the material by calcination in air flow in a tubular furnace at 600 °C for 6 h with a temperature ramp of 1 °C min^{-1}. The product is denoted SPC.

2.5 Synthesis of Ni^0/SPC

The nickel loading silica-pillared clay was synthesized as follows. The dry SPC was impregnated with nickel nitrate solution with a certain amount of nickel loading (40 mL of nickel nitrate solution to 1 g of SPC). Then the as prepared samples were reduced with a process as the Ni^{II}-SPC to Ni^0-SPC. The samples were named Ni^0/SPC-6, Ni^0/SPC-3 and Ni^0/SPC-2, according to the amount of nickel added in this process were 6%, 3% and 2%, respectively.

2.6 Characterization

X-ray powder diffraction (XRD) patterns were taken with a philips X'Pert diffractometer equiped with a rotating anode, using Cu-Kα radiation (λ = 0.1541 nm) in the 2θ range 5-70° with a scan speed of 10° min^{-1} and in the 2θ range 0.5-10° with a scan speed of 2° min^{-1}. High-resolution transmission electron microscopy (HRTEM) images were obtained by a JEM-3010 with an accelerating voltage of 200kV. The crystal morphology was studied using a Hitachi S-4700 scanning electron microscope (SEM). The nitrogen adsorption-desorption isotherms were measured at the liquid nitrogen temperature with a Quantachrome Autosorb-1 volumetric adsorption analyser. Prior to measurement, the samples were degassed at 300 °C for 16 h. The pore size distribution curves were calculated from the desorption branch of nitrogen adsorption-desorption isotherms. The X-ray photoelectron spectroscopy (XPS) analyses were conducted on an ESCALAB 250 spectrometer equipped with an Al Kα X-ray source. The carbon 1s peak at 284.6 eV was used as the reference for binding energies. Elemental analysis for Ni was performed using a Shimadzu ICPS-75000 inductively coupled plasma emission spectrometer (ICP-ES), an Elementar Vario EL elemental analyzer, and a PANalytical Axios Advanced wavelength dispersive X-ray fluorescence (WDXRF) spectrometer.

2.7 Catalytic performance test

The catalytic performance of the samples was tested through the reaction of HDC of CB. The experiments were carried out in a 250 mL stainless steel autoclave with ethanol as the solvent at the H_2 partial pressure of 1.5 MPa and with the reaction temperature of 100 ℃ for 1h. The percentage of reactant in the reaction system was 10 *wt.* %, and the catalyst dosage was 1.0 *wt.* %. The reactants and the products were analyzed by GC with a flame ionization detector online. And the conversion was calculated by the formula:

$$conversion(\%) = \frac{c_{C_6H_5Cl\,0} - c_{C_6H_5Cl\,i}}{c_{C_6H_5Cl\,0}} \times 100$$

$c_{C6H5Cl0}$ and $c_{C6H5Cli}$ denotes the molar concentration of CB before and after reaction, respectively.

To determine the turnover frequency (TOF), additional reactions with low chlorobenzene conversion (<15%) were tested. TOFs of catalysts at 70 °C are calculated as follows:

$$\mathrm{TOF} = \frac{\text{rate of chlorobenzene consumption}}{\text{No. of exposed Ni sites on catalyst}}\,^{[36]}.$$

The No. of exposed Ni sites on catalyst is calculated using the formula:

$$\text{No. of exposed Ni sites on catalyst} = W_{catalyst} \times \text{Percentage of Ni content} \times D$$

, where $W_{catalyst}$ is the weight of catalyst used in the catalytic reaction. And D is dispersion of Ni, which is calculated using the formula described by J. R. Anderson[37] :

$$D = \frac{\text{Ni}_{\text{ surface}}}{\text{Ni}_{\text{ total}}} = \left(\frac{4\pi r_1^2}{\pi r_2^2}\right) / \left(\frac{4/3\pi r_1^3}{V_2}\right) = \frac{3V_2}{\pi r_2^2 r_1}$$

r_1: radius of one nickel particle, r_2: radius of one nickel atom, V_2: volume of one nickel atom.

The nickel leaching analysis is also carried out as follows: the catalytic reaction is carried out for 1h, then the catalyst is separated by centrifugation. The solution without the catalyst is further stirred for 1h and the products in this solution and the products in this solution are determined. If the conversion of chlorobenzene is further improved without the presence of the catalyst, the nickel leaching is existence.

3. Results and discussion

View Article Online
DOI: 10.1039/C5RA05926G

3.1 Wide angle XRD patterns of the catalyst after reduction

In order to detect the phase of samples, wide angle XRD test was taken for all samples (Ni^0-SPCs) and the compared samples (Ni^0/SPCs).

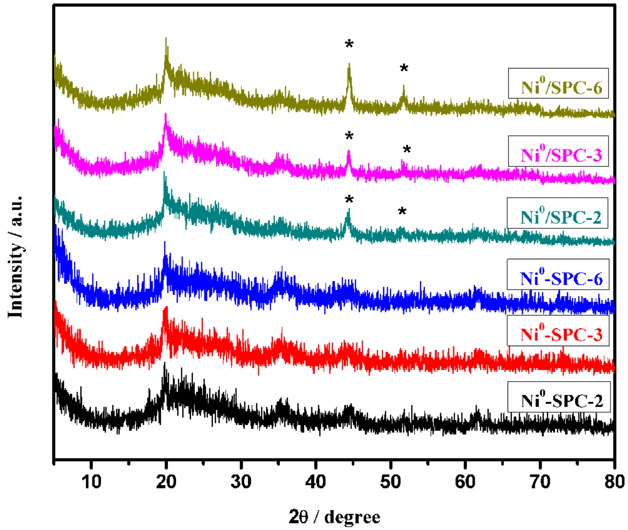

Fig.1 Wide angle XRD patterns of Ni^0/SPC-6, Ni^0/SPC-3, Ni^0/SPC-2, Ni^0-SPC-6, Ni^0-SPC-3 and Ni^0-SPC-2.

Fig.1 shows the wide angle XRD patterns of Ni^0/SPC-6, Ni^0/SPC-3, Ni^0/SPC-2, Ni^0-SPC-6, Ni^0-SPC-3 and Ni^0-SPC-2. In these patterns, all of samples are observed the typical peaks of MMT of its subgroup of 2:1 phyllosilicates, at 20°, 29°, and 35° and one weak broad feature at 62° 2θ[32]. This suggests that the MMT's structure of all of samples is not affected any more. The wide angle XRD pattern of natural MMT can be found in Fig.1S (ESI). However, there are some difference between Ni^0/SPCs and Ni^0-SPCs. At wide angle XRD patterns of Ni^0/SPCs, the two sharp peaks at 44.5°and 51.5° (asterisks marked) can be clearly seen. This indicates that the Ni^0 is present in the form of bulk Ni metal particles [38-40]. Correspondingly, for the Ni^0-SPCs, only one wide peak at about 44.5° can be seen and the peak at 51.5° is disappeared. The peak at 44.5° is characteristic of bulk nickel metal particles (1 1 1), which indicates that the nickel is still in the form of Ni metal particles. But the wide peak at 44.5° and the disappeared peak at 51.5° is the result of that the size of Ni metal particles are at the nano-scale [41].

3.2 TEM images of samples

In order to study the size of metal nickel particles and their distribution in Ni^0–SPCs and Ni^0/SPCs, the TEM of Ni^0–SPCs and Ni^0/SPCs with different nickel contents were employed. These results are shown in Fig.2.

The internal pore structures and nickel particle distributions of the as-prepared samples were observed by means of TEM. As is observed in Fig.2, the interlayer gallery pore structure is clearly evident. In the images, the clay layers are discernible as solid dark lines are the interlamellar pillars and the pores appear in lighter contrast between the layers[34,42]. For the Ni^0-SPCs, the metal nickel particles between the MMT layers which with an average diameter of 4.7 nm (measured on the basis of 200 particles) were distributed evenly around the silicon pillars in TEM images. However, the size of metal nickel particles in the Ni^0/SPCs would be much bigger with an average diameter of 26.4 nm (measured on the basis of 200 particles) comparing with the Ni^0-SPCs. From Fig.2A to Fig.2B and to Fig.2C, the number of metal nickel particles presented the law of diminishing, which is corresponding to the ICP-ES results that were given in Table 1. Furthermore, high-resolution transmission electron microscopy (HRTEM) provides more morphological information for nickel nanoparticles, as shown in Fig. 2B. The aligned lattice fringes of the nickel nanoparticles are clearly illustrated in the image with adjacent fringe spacing of about 0.20 nm, which is corresponding with the (1 1 1) diffraction we have observed at 2θ 44.5° of XRD.

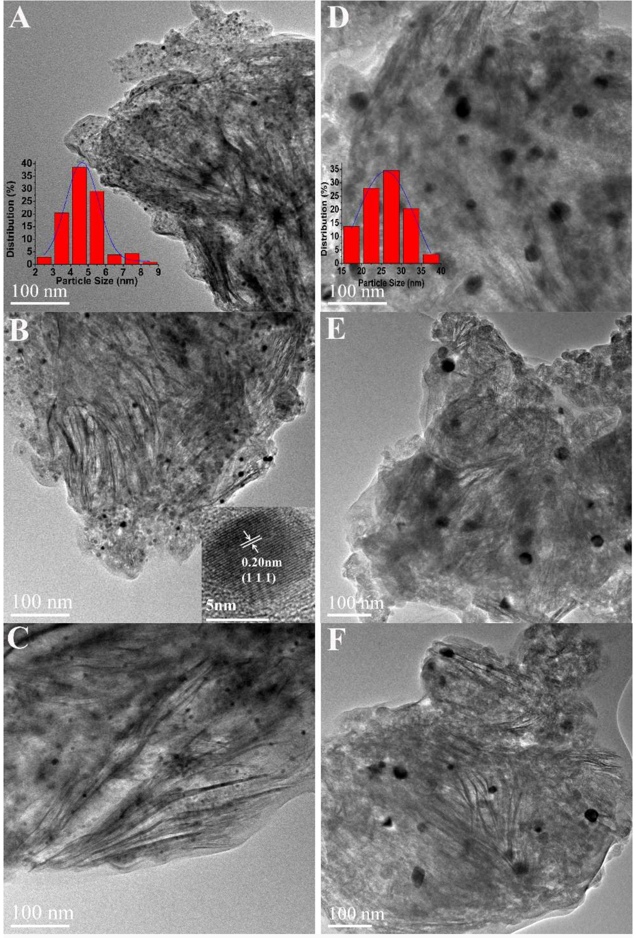

Fig.2 TEM images of samples with different nickel contents: (A) Ni^0-SPC-6, (B) Ni^0-SPC-3, (C) Ni^0-SPC-2 and (D) Ni^0/SPC-6, (E) Ni^0/SPC-3, (F) Ni^0/SPC-2.

3.3 Low angle XRD patterns of the catalyst after reduction

The pattern of an ordered lamellar clay material sample would usually exhibit one main peak (0 0 1) when recorded with a regular powder XRD. The order of (0 0 1) X-ray reflection, indicating layered structures, is observed for Ni^0-SPC-2, Ni^0-SPC-3 and Ni^0-SPC-6 with a basal spacing of 4.8 nm, 5.0 nm and 5.2 nm, and the gallery height of 3.8 nm, 4.0 nm and 4.2 nm after deducting the MMT layer thickness 0.96 nm respectively. The gallery height of Ni^0-SPCs is corresponding of that of Ni^{II}-SPCs, which can be seen in Fig. 2S (ESI). This indicates that the Ni-SPCs still possess the lamellar structure. But the strength of peak is a little weaker and

View Article Online
DOI: 10.1039/C5RA05926G

Table 1. ICP-ES results and textural properties of Ni^{0}-SPCs and Ni^{0}/SPCs.

Sample	Si/Ni	Ni content tested by ICP-ES (*wt.* %)	BET (m^2g^{-1})	Total pore volume (cm^3g^{-1})	Mesopore diameter (nm)
Ni^{0}-SPC-6	10	5.68	476	0.496	3.81
Ni^{0}-SPC-3	20	2.75	471	0.421	3.43
Ni^{0}-SPC-2	30	1.83	451	0.380	3.27
Ni^{0}/SPC-6	10	5.89	520	0.460	3.25
Ni^{0}/SPC-3	20	2.91	517	0.452	3.18
Ni^{0}/SPC-2	30	1.90	490	0.458	3.17

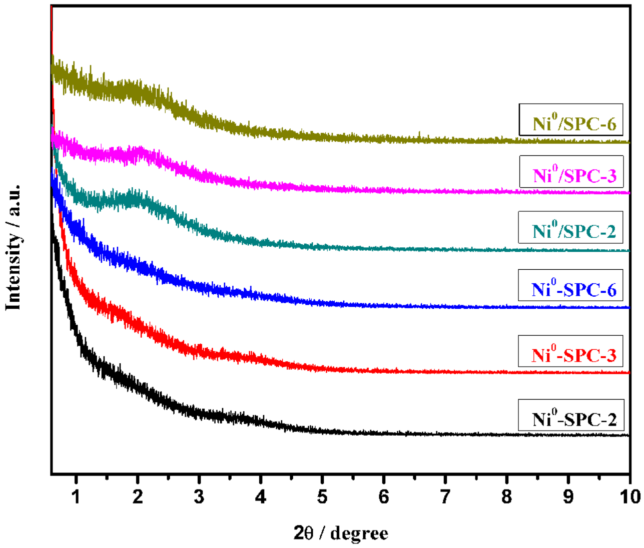

Fig.3 Low angle XRD patterns of Ni^{0}/SPC-6, Ni^{0}/SPC-3, Ni^{0}/SPC-2, Ni^{0}-SPC-6, Ni^{0}-SPC-3 and Ni^{0}-SPC-2.

the width become wider, which infers that the structure of the interlamellar pillars has been changed during the reduction process. The order of (0 0 1) X-ray reflection is also observed for Ni^{0}/SPC-2, Ni^{0}/SPC-3 and Ni^{0}/SPC-6 with a basal spacing about 4.4 nm and the gallery height of 3.4 nm after deducting the MMT layer thickness 0.96 nm. Compared with the change between Ni^{II}-SPCs and Ni^{0}-SPCs, it infers that the silica pillar in the Ni^{0}/SPCs is not affected any more.

3.4 SEM images of samples

The morphologies of the as-prepared samples were observed by means of SEM. It is observed that except for the detailed roughness of surfaces, the overall morphology of the MMT layer was well retained when the Ni^{0} -SPC samples were just completed. As it is shown in Fig.4C, for the Ni content was in a very low condition, the morphology of the as-prepared sample was very similar to that of SPC (Fig.3S in ESI). With the increase of nickel content in the Ni^{0} -SPC, the surface of clay sheets became rougher (Fig.4B). When the nickel content was in a highest condition (Fig.4A), there was even little amorphous SiO_2 particles can be observed on the surface of clay sheets in Ni^{0}-SPC sample. This phenomenon may be due to the fact that most of the TEOS hydrolysis occurred in the gallery regions of MMT under such intercalation condition. However, the addition of too much nickel would affect the regularity of the Ni^{0}-SPC material.

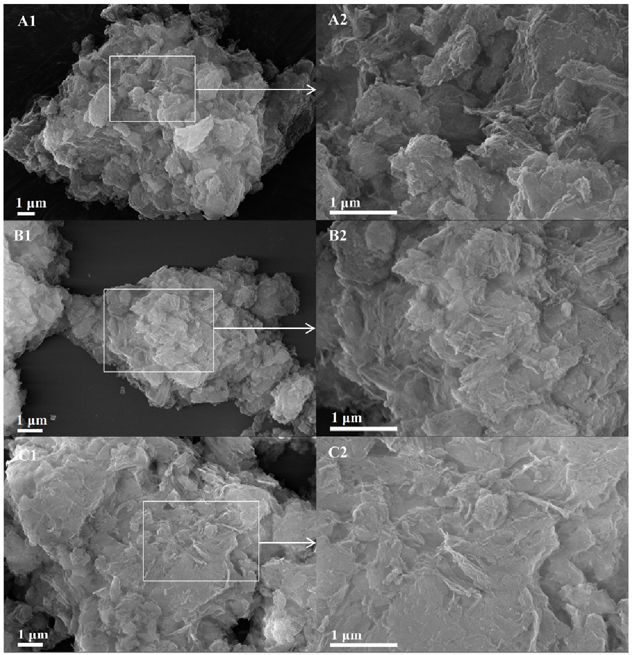

Fig. 4 SEM images of (A) Ni^{0}-SPC-6, (B) Ni^{0}-SPC-3, (C) Ni^{0}-SPC-2.

3.5 N_2 adsorption-desorption analysis of the samples

Fig.5 shows the nitrogen adsorption-desorption isotherms and the pore size distribution curves (calculated from the desorption branch) of Ni^{0}-SPCs and Ni^{0}/SPCs. For all of these materials, the uptake of nitrogen increased linearly with pressure between 0.03 and 0.8, and a jump of nitrogen uptake was observed above 0.8. The curve is categorized as the type IV isotherm according to the BDDT (Brunauer -Deming - Deming - Teller) classification with a hysteresis loop, whose features correspond to the type B in Boer's five types representing the presence of open slit-shaped pores formed in gallery regions. The adsorption isotherm and the hysteresis loop are contributed by mesopores and slit-shaped spacing in gallery cooperatively. The Ni^{0}/SPCs have BET specific areas of 490-520 m^2/g and pore volumes of 0.452-0.460 cm^3g^{-1}. However, the BET specific areas of Ni^{0}-SPCs were a little smaller compared with that of Ni^{0}/SPCs, being 451-476 m^2/g. And the pore volumes of Ni^{0}-SPCs were 0.380-0.496 cm^3g^{-1}.

The pore size distribution curve of Ni^{0}-SPC-2 shows that the narrow pore size distribution is similar with MCM-41, which possess mesopores produced by surfactant micelles. This

View Article Online
DOI: 10.1039/C5RA05926G

indicates that the samples were well-ordered mesostructure materials and probably produced by surfactant micelles. Meanwhile, for Ni^0-SPCs, with the nickel content increasing, the pore size, pore volume and the surface area are increasing (Table 1). This is because with the increase of nickel content in the samples, the content of metallic nickel particles between the MMT layers increases, so that the spacing of MMT layer enlarges, and more space is formed, which is corresponding with the low-angle XRD results of Ni^0-SPCs. However, the pore size distribution curves of Ni^0/SPCs were very similar, with a pore size distribution of 3.17-3.25 nm, indicating that the pore structure of SPC was not changed after nickel was loaded.

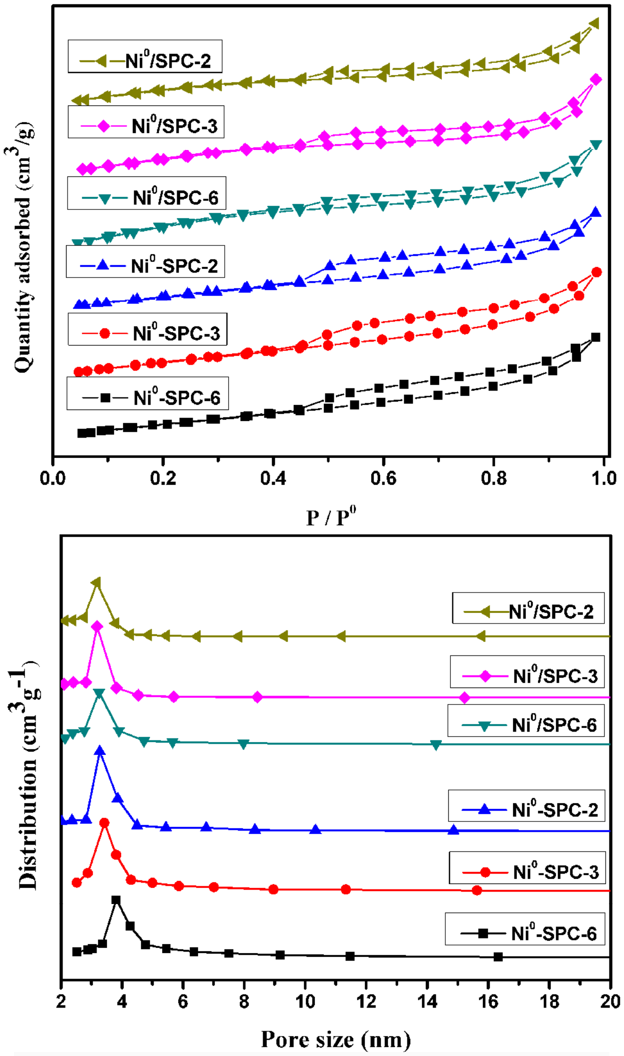

Fig.5 N_2 adsorption-desorption and pore size distributions of Ni^0/SPC-6, Ni^0/SPC-3, Ni^0/SPC-2, Ni^0-SPC-6, Ni^0-SPC-3 and Ni^0-SPC-2.

3.6 XPS test of the samples

In order to explore the state of Ni material, the XPS spectrum is employed. The results are shown in the Fig. 6.

As shown in Fig. 6, the two strong peaks at 856.2 and 874.6 eV are correspond to $Ni^02p_{3/2}$ and $Ni^02p_{1/2}$, respectively. And the peaks appeared at 863.6 and 881.0 eV are attributed to the $Ni^{2+}2p_{3/2}$ and $Ni^{2+}2p_{1/2}$, respectively. The peaks of Ni^0 2p and Ni^{2+} 2p are shift to higher energies compared with the reported oxidation state of Ni^0 and Ni^{2+}, maybe due to the electronegative of montmorillonite lamellar and the interaction between Ni atom and silica of SPC interlamellar.

At the same time, the BE value of the Si2p and O1S decrease to 103.2 and 532.0 eV, respectively, compared with the reported oxidation state of silica and SPC[43]. This might be due to the Ni-O-Si bonds between the Ni atom of nickel nanoparticles and the framework of SPC, which causes a decrease of the density of the lining electron cloud of the oxygen and silicon atoms.[44]

3.7 FTIR patterns of as-prepared samples

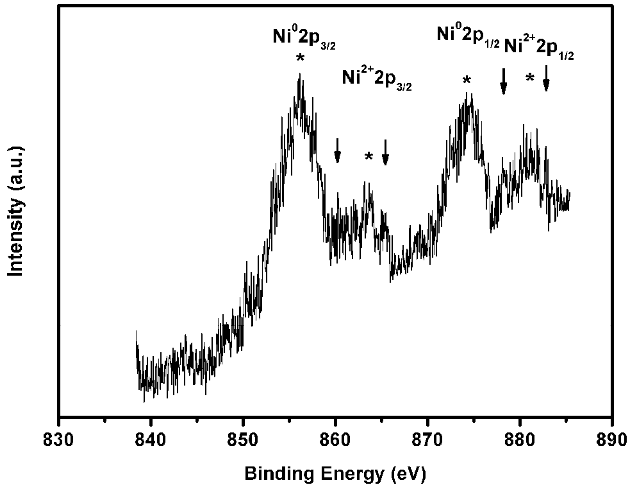

Fig. 6 XPS spectrum of Ni^0-SPC-6 (Asterisks indicate Ni 2p peaks and arrows are the peak positions of Ni^0 and Ni^{2+} satellite peaks).

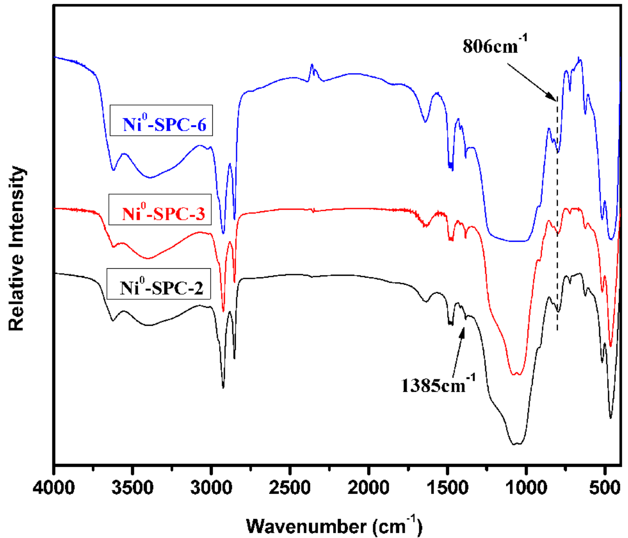

Fig.7 FTIR patterns of Ni^0-SPC-6, Ni^0-SPC-3 and Ni^0-SPC-2.

Fig. 7 shows the FTIR spectra of the products in the range of 4000-450 cm^{-1}. The strong and wide bands around 1200-1000 cm^{-1} are associated to the asymmetric Si–O stretching modes. The intensity of the band at 1385 cm^{-1} (Ni–O–Si bond) has become much weaker comparing with the band of Ni^{II}-SPCs at 1385 cm^{-1}(Fig.4S in ESI). Moreover, the characteristic bands in 806 cm^{-1} could be observed for all the samples, which is a slight blue-shift comparing with the shift of Ni^{II}-SPCs in 803 cm^{-1}. This can be contributed to the fact that as most of the Ni atoms were reduced from the framework of SPC, the Ni-O-Si

View Article Online
DOI: 10.1039/C5RA05926G

bonds were destroyed[43,45]. However, the reduction process is not complete, leading to a small part of the Ni−O−Si bonds exist in the samples, which is the reason that nickel particles were fixed between the interlayer of Ni^0-SPCs.

3.8 Catalytic performance test

The reaction of HDC of CB was carried out using the Ni^0-SPCs and the Ni^0/SPCs as catalysts under the same conditions. Normally, HDC of CB results in the production of three products: benzene, cyclohexane, and chlorocyclohexane. But in this catalytic performance test, by using the Ni^0-SPCs as catalyst, the only detected product is benzene and there are not cyclohexane and chlorocyclohexane at all. The reason to lead this result can be attributed not only to the lower reaction temperature than that of the previous reports, but also to the high ordered pore structure of SPC. The catalytic performances are shown in Fig.8.

Fig.8 shows the conversion of chlorobenzene to benzene with different nickel contents of Ni^0-SPCs and Ni^0/SPCs. It can be observed that the Ni^0-SPCs show better conversion of chlorobenzene to benzene in this catalytic reaction than the Ni^0/SPCs did. The conversions of CB increase from 74.1% to 83.6% and finally to 97.8% as the nickel contents of the Ni^0-SPC-i increase from 2% to 3% and to 6%. And this is much better than 57.2%, 62.1%, 70.1% over the corresponding sample Ni^0/SPC-i (i=2, 3, 6), respectively. The Ni^0-SPC-i samples exhibited much higher catalytic activity than the Ni^0/SPC-i samples, which can be attributed to the much smaller nickel nanoparticles with high dispersion in an ordered distribution manner in the high ordered pore structure of SPC.

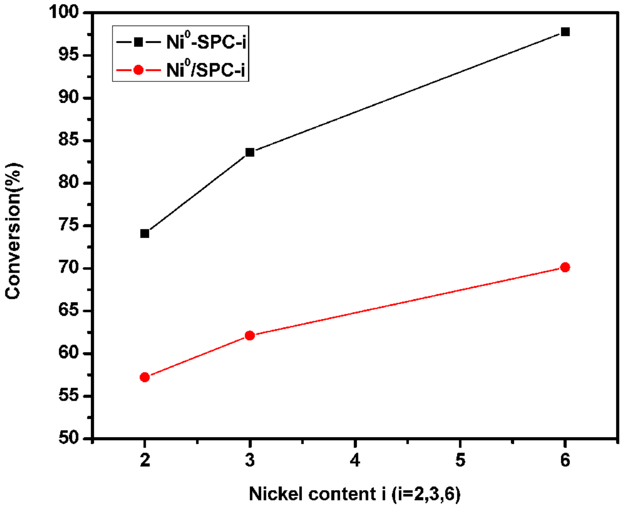

Fig.8 Conversion of chlorobenzene to benzene with Ni^0-SPC-i or Ni^0/SPC-i as catalyst (i=2, 3, 6).

The reusability of Ni^0-SPC-6 and Ni^0/SPC-6 were also examined under the same conditions, and the results are shown in Fig.9.

Fig.9 shows the reusability of Ni^0-SPC-6 and Ni^0/SPC-6. It can be observed that after five times of catalytic reaction, the conversion of CB with Ni^0/SPC-6 as catalyst was still 94.1%, which is only 3.7% lower corresponding with the first time. However, the catalytic performance of Ni^0/SPC-6 had significant decrease after four runs, and the conversion of CB was only 46.6% in the fifth time. These data significantly indicate that the reusability of Ni^0-SPC-6 was much better than that of Ni^0/SPC-6.

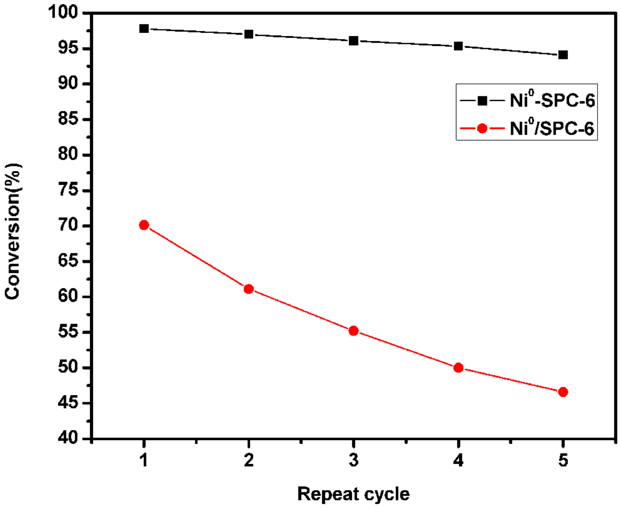

Fig.9 Reusability of Ni^0-SPC-6 and Ni^0/SPC-6.

TOF, as the intrinsic activity of the reaction, is calculated at 70 °C and is expressed as the rate of chlorobenzene consumption per number of exposed Ni sites on the catalyst. The TOF value of Ni^0-SPC-6 (0.0897s^{-1}) is comparable to that of Ni^0/SPC-6 (0.1278s^{-1}) under similar reaction conditions, but do vary somewhat with the nickel dispersion. This indicates that the highly dispersion of Ni in Ni^0-SPC-6 leading to the good catalytic activity of chlorobenzene to benzene.

The Koros−Nowak test is an effective method to identify heat or mass transfer limitations in the measurement of catalytic rates[46,47]. If the observed TOFs of catalysts with different metal loadings are the same, this means that there are no heat or mass transfer limitations under the tested conditions. Therefore, a Koros−Nowak test was carried out on catalysts with similar dispersion but different nickel contents at 70 °C. As shown in Figure 10, the values of TOF remain almost unchanged under the same reaction conditions when altering the nickel contents, demonstrating that there are no heat or mass transfer limitations under this condition.

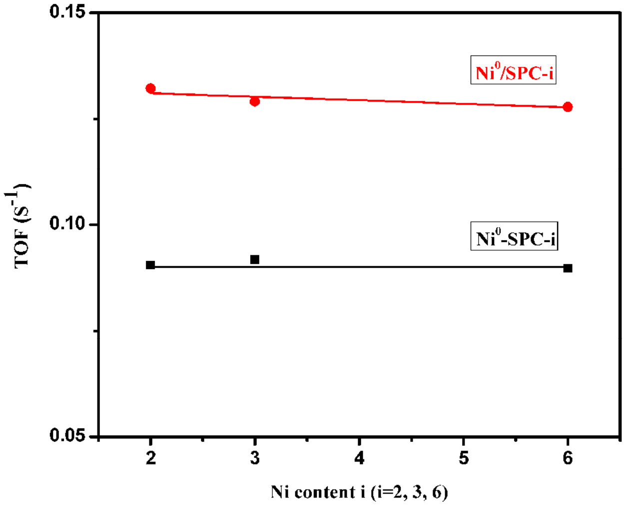

Fig. 10 TOFs of Ni^0-SPC-i o and Ni^0/SPC-i (i=2, 3, 6).

The nickel leaching analysis of Ni^0-SPC-6 and Ni^0/SPC-6 were carried out after their fifth times of catalytic reaction. The result shows that after another hour of reaction, conversion of chlorobenzene in the Ni^0-SPC-6 reaction system did not further improve, indicating no nickel leaching of Ni^0-SPC-6. However, the conversion of chlorobenzene in the Ni^0/SPC-6 was improved after another hour of reaction without catalyst. This indicates that after five times of reaction, the nickel of Ni^0/SPC-6 was leached out. The

View Article Online
DOI: 10.1039/C5RA05926G

samples were also analysed by ICP-ES, showing that the nickel content of Ni^0-SPC-6 after the five times of reaction was 5.63%, nearly the same as that before reaction (5.68%), however, the nickel content of Ni^0/SPC-6 after five times of reaction was 4.27%, much lower compared with that before reaction (5.89%).

In order to investigate the distribution of nickel particles after five times of catalytic reaction, the Ni^0-SPC-6 and Ni^0/SPC-6 were analysed by TEM, and the results are shown in Fig. 5S. As is observed in Fig.5S, for Ni^0-SPC-6, the metal nickel particles with an average diameter of 5.4 nm (measured on the basis of 200 particles) were distributed evenly between the MMT layers. The average diameter of nickel particles was increased 0.7 nm after five times of catalytic reaction (the average diameter of nickel particles of Ni^0-SPC-6 before catalytic reaction was 4.7 nm, which can be found in Fig.2). The largest particles we have observed were about 13 nm, which was increased 4 nm after five times of catalytic reaction. Because of the strong interaction between the nickel particles and the SPC supporter, the nickel particles were prevented from aggregation, leading to a good reusability in the catalytic reaction. For Ni^0/SPC-6, the average diameter of metal nickel particles was 31.2 nm (measured on the basis of 200 particles) after five times of catalytic reaction, which was increased 4.8 nm than that before the catalytic reaction (the average diameter of nickel particles of Ni^0/SPC-6 before catalytic reaction was 26.4 nm, which can be found in Fig.2). The biggest particles we have observed were more than 50 nm, which was increased 10 nm after five times of catalytic reaction. The increase of diameter of nickel particles indicates that the nickel particles of Ni^0/SPC-6 were aggregated after five times of catalytic reaction, which is in accordance with some other support catalysts published previous[48,49].

Above all, the enhanced stability of the Ni^0-SPC-i samples is consistent with the smaller crystallite size, higher nickel dispersion, higher ordered distribution of the nickel nanoparticles, and the stronger interaction between the nickel species and the SPC supporter.

3.9The formation mechanism of Ni^0-SPC

According to the aforementioned observations, we propose a mechanism (Scheme 1) to explain the formation of Ni^0-SPCs.

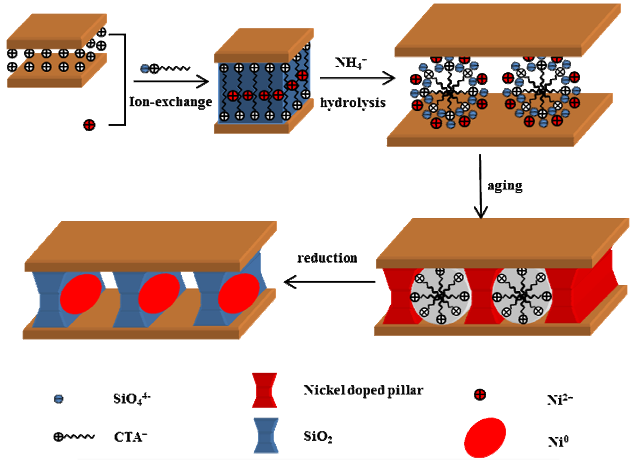

Scheme 1. The formation mechanism of Ni^0-SPC.

The mixture of the MMT, Ni^{2+}, CTA^+, and TEOS resulted in swollen gel, allowing the formation of intercalation compound in which Ni^{2+}, CTA^+ and TEOS are simultaneously intercalated into the interlayer space of MMT. Here, Ni^{2+} and CTA^+ are intercalated into clay interlayers by ion exchange and TEOS is introduced into clay interlayered space by solvation. The intercalation process also results in the expansion of the interlayer space of MMT. After liquid crystal assembling of the gels, when ammonium was added into the gel mixture, there were two important processes occurs in the clay interlayer space. (1) The nickel-ammonia complex was formed immediately and adsorbed into the interlayer space by cationic surfactant. (2) The hydrolysis of the TEOS occurs rapidly around the molecular micelles which the CTA^+ forms. During the hydrolysis process, nickel-ammonia complex was incorporated into SiO_2 frame and formed the nickel doped pillars of Ni^{II}-SPC.

Finally, the mesoporous material with unify pore structure was successfully synthesized through a direct synthesis method and all the Ni(II) ions were uniformly dispersed in the silica framework. After the Ni(II) species were reduced to Ni(0), the metallic Ni(0) atoms would transfer along with the channel to form nickel atom clusters and then become nickel particles. Because of the strong restrictive effect of the framework of SPC, the nickel particle diameters were restricted and hard to form big nickel particles under the experimental conditions. Meanwhile, those Ni metal particles is almost anchored on the framework of SPC, because there may be trace of Ni atoms on the Ni metal particles that they are not reduced to the Ni^0 and they are still related with the silica pillar.

4. Conclusion

In summary, a series of highly dispersed nickel nanoparticles between the lamellae of silica pillared clay have been synthesized with a facile process. The high degree of Ni^{II} dispersion in the Ni^{II}-SPC precursor induces a good distribution of Ni nanoparticles and prevents their aggregation by anchoring on the framework. The highly dispersed nickel nanoparticles with a uniform size about 4.7 nm and narrow size distribution are in an ordered configuration between the lamellae of silica pillared clay. Moreover, the materials possess highly ordered mesoporous structure with high specific surface area and large pore volume. And the nickel catalysts exhibit high catalytic performance and good reusability on the hydrodechlorination of chlorobenzene.

Notes and references

[1] State Key Laboratory of Chemical Resource Engineering, Beijing University of Chemical Technology, No. 15 Bei-sanhuan East Road, Beijing 100029, P. R. China.

[2] Zhengzhou University of Light Industry, No. 5 Dongfeng Road, Zhengzhou, Henan Province 450002,P. R. China.

[3] Beijing Institute of Aerospace Testing Technology.

[4] No. 153 Central Hospital of Chinese PLA, Zhengzhou, Henan Province 450007, P. R. China.

[5] Yanshan branch of Beijing Research Institute of Chemical Industry, No. 15 Fenghuangting Road, Beijing 102500, P. R. China.

[6] Henan Radio&Television University, No. 124 Huanghe Road, Zhengzhou, Henan Province 450000, P. R. China.

Electronic Supplementary Information (ESI) available: [Wide angle XRD patterns of SPC and MMT; TEM images of MMT, SPC and Ni^{II}-SPC-6; Low angle XRD patterns of Ni^{II}-SPCs; SEM images of SPC, Ni^0/SPC-6, Ni^0/SPC-3, and Ni^0/SPC-2; FTIR patterns of Ni^{II}-SPC-6, Ni^{II}-SPC-3, Ni^{II}-SPC-2, SPC and MMT.] See DOI: 10.1039/b000000x/

1 Y. Mei, G. Sharma, Y. Lu and M. Ballauff, *Langmuir*, 2005, ***21***, 12229-12234.

View Article Online
DOI: 10.1039/C5RA05926G

2 Z. Chen, C. D. Pina, E. Falletta, M. L. Faro, M. Pasta, M. Rossi and N. Santo, *J. Catal.*, 2008, ***259***, 1-4.

3 Y.-C. Liu and Y.-W. Chen, *Ind. Eng. Chem. Res.*, 2006, ***45***, 2973-2980.

4 G. J. Hutchings, *Catal. Today*, 2005, ***100***, 55-61.

5 M. M. Telkar, C. V. Rode, R. V. Chaudhari, S. S. Joshi and A. M. Nalawade, *Appl. Catal.*, *A*, 2004, ***273***, 11-19.

6 M. J. Vaidya, S. M. Kulkarni and R. V. Chaudhari, *Org. Process Res. Dev.*, 2003, ***7***, 202-208.

7 A. M. Signori, K. O. Santos, R. Eising, B. L. Albuquerque, F. C. Giacomelli and J. B. Domingos, *Langmuir*, 2010, ***26***, 17772-17779.

8 Y. Lu, Y. Mei, M. Schrinner, M. Ballauff, M. W. Moller and J. Breu, *J. Phys. Chem. C*, 2007, ***111***, 7676-7681.

9 Z. Zhu, X. Guo, S. Wu, R. Zhang, J. Wang and L. Li, *Ind. Eng. Chem. Res.*, 2011, ***50***, 13848-13853.

10 M. H. Rashid and T. K. Mandal, *J. Phys. Chem. C*, 2007, ***111***, 16750-16760.

11 Z. Jiang, J. Xie, D. Jiang, X. Wei and M. Chen, *CrystEngComm*, 2013, ***15***, 560-569.

12 N. Wu, W. Zhang, B. Li, C. Han, *Micropor. Mesopor. Mater.*, 2014, ***185***, 130-136.

13 J. C. Park, J. U. Bang, J. Lee, C. H. Ko and H. Song, *J. Mater. Chem.*, 2010, ***20***, 1239-1246.

14 A. Nandi, M. D. Gupta and A. K. Banthia, *Mater. Lett.*, 2002, ***52***, 203-205.

15 W. Xu, K. Y. Liew, H. Liu, T. Huang, C. Sun and Y. Zhao, *Mater. Lett.*, 2008, ***62***, 2571-2573.

16 D. H. Chen and C. H. Hsieh, *J. Mater. Chem.*, 2002, ***12***, 2412-2415.

17 M. L. Singla, A. Negi, V. Mahajan, K. C. Singh and D. V. S. Jain, *Appl. Catal., A*, 2007, ***323***, 51-57.

18 K. H. Kim, Y. B. Lee, S. G. Lee, H. C. Park and S. S. Park, *Mater. Sci. Eng., A*, 2004, ***381***, 337-342.

19 D. S. Sidhaye, T. Bala, S. Srinath, H. Srikanth, P. Poddar, M. Sastry and B. L. V. Prasad, *J. Phys. Chem. C*, 2009, ***113***, 3426-3429.

20 R. P. -Hernandez, G. M. -Galicia, A. A. Maravilla and J. Palacios, *Phys. Chem. Chem. Phys.*, 2013, ***15***, 12702-12708.

21 Y. Kim, P. Kim, C. Kim and J. Yi, *J. Mater. Chem.*, 2003, ***13***, 2353-2358.

22 Y. Li, J. Wang, X. Wang and J. Wang, *Ind. Eng. Chem. Res.*, 2012, ***51***, 6520-6528.

23 Z. Zhang, S. Saengkerdsub and Sheng Dai, *Chem. Mater.*, 2003, ***15***, 2921-2925.

24 J. Lin, J. Wei and W. Tsai, *J. Phys. Chem. B*, 2007, ***111***, 10275-10280.

25 M. Polverejan, T. R. Pauly and T. J. Pinnavaia, *Chem. Mater.*, 2000, ***12***, 2698-2704.

26 M. Pichowicz and R. Mokaya, *Chem. Commun.*, 2001, ***20***, 2100-2101.

27 J. Lin, T.-Y. Juang, *Polymer*, 2004, ***45***, 7887-7893.

28 A. Galarneau, A. Barodawalla, J. T. Pinnavaia, *Nature*, 1995, ***374***, 529-531.

29 H. Mao, B. Li, X. Li, L. Yue, Z. Liu, W. Ma, *Ind. Eng. Chem. Res.*, 2010, ***49***, 583-591.

30 H. Mao, X. Liu, J. Yang, B. Li, Q. Chen, J. Zhong, *Micropor. Mesopor. Mater.*, 2014, ***184***, 169-176.

31 H. Mao, X. Lu, M. Li, J. Yang, B. Li, *Appl. Surf. Sci.*, 2013, ***276***, 787–795.

32 H. Mao, B. Li, X. Li, Z. Liu, W. Ma, X. *Catal. Commun.*, 2009, ***10***, 975-980.

33 H. Mao, X. Gao, J. Yang, B. Li, *Appl. Surf. Sci.*, 2011, ***257***, 4655–4662.

34 H. Mao, B. Li, X. Li, L. Yue, J. Xu, B. Ding, X. Gao, Z. Zhou, *Micropor. Mesopor. Mater.*, 2010, ***130***, 314-321.

35 H. Mao, B. Li, X. Li, Z. Liu, W. Ma, *Materials Research Bulletin*, 2009, ***44***, 1569-1575.

36 Y. Li, B. W.L. Jang, *Applied Catalysis A: General*, 2011, ***392***, 173-179.

37 J. R. Anderson, *Structure of Metallic Catalysts*, Academic Press, London, 1975.

38 V. C. S. Palla, D. Shee and S. K. Maity, *RSC Adv.*, 2014, ***4***, 41612-41621.

39 W. Jiao, X. Hu, H. Ren, P. Xu, R. Yu, J. Chen and X. Xing, *J. Mater. Chem. A*, 2014, ***2***, 18171-18176.

40 P. S. Roy and S. K. Bhattacharya, *RSC Adv.*, 2014, ***4***, 13892-13900.

41 H. Zhang, D. Pan, and X. Duan, *J. Phys. Chem. C*, 2009, ***113***, 12140-12148.

42 M. Polverejan, T. R. Pauly and T. J. Pinnavaia, *Chem. Mater.* 2000, ***12***, 2698-2704.

43 L. Yue, B. Li, Z. Ren, N. Wu and X. Li, *Chemistry Letters*, 2014, ***43***, 1473-1475.

44 R. Akbarzadeh and H. Dehghani, *Dalton Trans.*, 2014, ***43***, 5474-5481.

45 D. Rath and K. M. Parida, *Ind. Eng. Chem. Res.*, 2011, ***50***, 2839-2849.

46 J. Xu, L. Ouyang, W. Mao, X. J. Yang, X. C. Xu, J. J. Su, T. Z. Zhuang, H. Li, Y. F. Han, *ACS Catal.*, 2012, ***2***, 261-269.

47 Y. F. He, J. T. Feng, Y. Y. Du and D. Q. Li, *ACS Catal.*, 2012, ***2***, 1703-1710.

48 Y. F. He, L. L. Liang, Y.Y. Liu, J. T. Feng, C. Ma, D. Q. Li, *J, Catal.* 2014, ***39***, 166-173.

49 D. Kumar and A. Ali, *Energy Fuel*, 2013, ***27***, 3758-3768.